Nanoscale

PAPER

View Article Online
View Journal | View Issue

Cite this: *Nanoscale*, 2018, **10**, 1256

In vivo formation of protein corona on gold nanoparticles. The effect of their size and shape†

Rafaela García-Álvarez,[a,b] Marilena Hadjidemetriou,[a] Ana Sánchez-Iglesias,[b] Luis M. Liz-Marzán[*b,c,d] and Kostas Kostarelos[*a]

Received 8th November 2017,
Accepted 4th December 2017

DOI: 10.1039/c7nr08322j

rsc.li/nanoscale

The efficacy of drug delivery and other nanomedicine-related therapies largely relies on the ability of nanoparticles to reach the target organ. However, when nanoparticles are injected into the bloodstream, their surface is instantly modified upon interaction with blood components, principally with proteins. It is well known that a dynamic and multi-layered protein structure is formed spontaneously on the nanoparticle upon contact with physiological media, which has been termed *protein corona*. Although several determinant factors involved in protein corona formation have been identified from *in vitro* studies, specific relationships between the nanomaterial synthetic identity and its ensuing biological identity under realistic *in vivo* conditions remain elusive. We present here a detailed study of *in vivo* protein corona formation after blood circulation of anisotropic gold nanoparticles (nanorods and nanostars). Plasmonic gold nanoparticles of different shapes and sizes were coated with polyethyleneglycol, intravenously administered in CD-1 mice and subsequently recovered. The results from gel electrophoresis and mass spectrometry analysis revealed the formation of complex protein coronas, as early as 10 minutes post-injection. The total amount of protein adsorbed onto the particle surface and the protein corona composition were found to be affected by both the particle size and shape.

Introduction

In the context of nanomedicine it is crucial to understand (and ideally control) the fate of nanoparticles upon administration in the human body. Among other effects that can determine their biodistribution, the surface chemistry of NPs plays a major role in the colloidal stability, as well as in the interactions with cell membranes and other biological entities. Even though surface chemistry can be tailored during or after synthesis, it is well established that proteins and other biomolecules present in biological fluids can potentially adsorb onto the surface of NPs. Proteins in particular are known to readily adsorb on NPs, forming a coating shell that is known as the "protein corona",[1] and is currently recognized as a major element in modulating the bioidentity of NPs and hence, their overall pharmacological and toxicological profile.[2–4] In other words, the biological identity of a nanomaterial will be largely affected by the composition of the protein corona, which in turn strongly depends on both the nanomaterial synthetic identity[5–8] and the physiological environment.[9–12] Numerous studies have been conducted to mechanistically understand the dynamic process of protein corona formation, its kinetic evolution and its dependence on the synthetic physicochemical properties of the NPs.[13] Highly relevant parameters are the NP size and shape, surface charge, surface functionalization and hydrophobicity.[14]

Among the wide variety of existing nanomaterials, gold nanoparticles (AuNPs) have attracted extensive attention due to their interesting optical (plasmonic) properties, which can be tuned by simply modifying the size and shape of the NPs.[15,16] The ability of (anisotropic) AuNPs to absorb and scatter light in the visible and near-IR with very high efficiency can be potentially exploited for different biomedical applications,[17,18] including diagnosis, imaging and therapy, which in some cases have even reached clinical trials.[19] Taking into consideration that the composition and properties of the protein corona greatly depend on the physicochemical properties of nanomaterials, numerous studies have been devoted to understanding the influence of the synthetic identity of AuNPs on the composition and biological impact of the resulting protein corona.[20,21] In the particular case of AuNPs, the morphological details (size and shape) are crucial toward opti-

[a]*NanomedicineLab, Faculty of Biology, Medical & Health, The University of Manchester, Manchester M13 9PT, UK. E-mail: kostas.kostarelos@manchester.ac.uk*
[b]*Bionanoplasmonics Laboratory, CIC biomaGUNE, Paseo de Miramón 182, 20014 Donostia-San Sebastián, Spain. E-mail: llizmarzan@cicbiomagune.es*
[c]*Ikerbasque, Basque Foundation for Science, 48013 Bilbao, Spain*
[d]*Ciber de Bioingeniería, Biomateriales y Nanomedicina, Ciber-BBN, 20014 Donostia-San Sebastián, Spain*

†Electronic supplementary information (ESI) available. See DOI: 10.1039/c7nr08322j

mizing their plasmonic properties, such as plasmon modes in the near-IR (biological transparency window), which can be obtained by introducing anisotropy. In this respect, elongated (nanorods) and spiky (nanostars) AuNPs have been proposed as preferred morphologies for biomedical applications. Interestingly, although the NP shape is also thought to play an important role in protein corona formation, few studies have been devoted to determining the effect of shape on the protein corona composition.[22,23] Investigations on protein corona formation and properties have mainly focused on spherical AuNPs,[24–26] whereas recent publications also report protein corona studies on AuNPs of different geometries, including nanorods[27,28] and nanostars.[29] However, to the best of our knowledge, comparative studies of protein corona formation on AuNPs with different morphologies have not been reported.

Another important limitation is posed by the *in vitro* design of the experiment to study the interaction between NPs and biofluids, which fails to recognize the highly dynamic nature of blood and its heterogeneous flow velocity.[30] Some of us recently reported a protocol that allows us to recover clinically-used, lipid-based NPs from the blood circulation of rodents after intravenous administration, so as to investigate the *in vivo* protein corona formation, as well as its evolution.[31,32] The methodology utilized for the isolation of the protein corona–NP complex was based on a combination of size exclusion chromatography and membrane ultrafiltration, which demonstrated that the molecular complexity and morphology of the *in vivo* protein corona cannot be adequately predicted by the *in vitro* plasma incubation of NPs.

We have now implemented a similar method to comprehensively characterize and compare protein corona fingerprints formed *in vivo*, on the surface of AuNPs coated with polyethyleneglycol (PEG). We thereby investigated the effect of size and shape on the formation of the protein corona under *in vivo* blood flow conditions. Gold nanorods (AuNRs) and gold nanostars (AuNSs) with overall sizes of 40 and 70 nm were intravenously administered and recovered from the blood circulation of CD-1 mice, and the *in vivo* formed protein coronas were qualitatively and quantitatively characterized by high-resolution liquid chromatography coupled to mass spectrometry (LC-MS) based proteomics.

Results and discussion

The synthesis of AuNRs and AuNSs was based on extensively reported seeded growth methods,[33–36] followed by functionalization with thiolated PEG (M_w = 10 kDa) containing carboxylic acid end-functional groups. The initial characterization of the AuNPs used in this study is summarized in Fig. 1 and 2, and Table S1 (ESI†). Dynamic light scattering (DLS), ζ-potential, UV-Visible spectroscopy and transmission electron microscopy (TEM) measurements were performed prior to intravenous administration of AuNPs, to assess their properties and morphology. The TEM images revealed well dispersed NPs of the following dimensions: AuNRs of 40 × 11 and 70 × 15 nm and

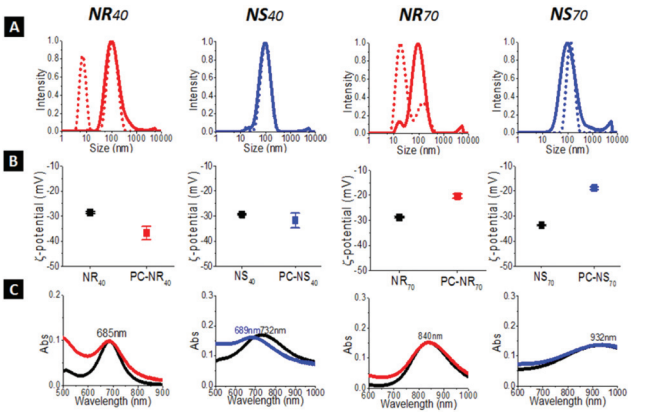

Fig. 1 The effect of PC formation on the physicochemical properties of AuNPs. DLS size distribution (A), ζ-potential (B) and UV-vis-NIR extinction spectra (C) are depicted for AuNRs and AuNSs before (dotted lines) and after (solid lines) interaction with CD-1 mouse plasma *in vivo*. ζ-potential values are given before (black) and after (red/blue) PC formation, error bars refer to the standard deviation.

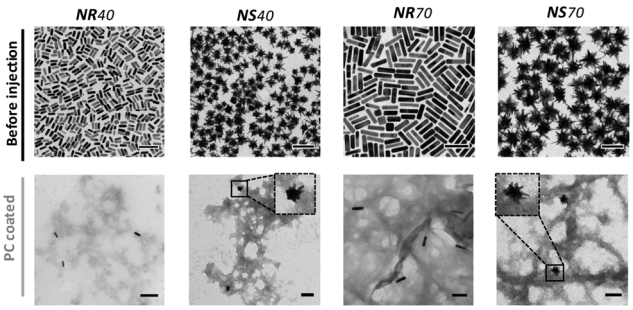

Fig. 2 Representative TEM images of AuNRs and AuNSs (as labelled), before (upper panel) and after (lower panel) interaction with CD-1 mouse plasma *in vivo*.

AuNSs of 40 and 70 nm external diameter (see the Experimental section for details). DLS measurements of AuNSs show a single peak for the hydrodynamic diameter (HD), whereas AuNRs exhibited two different peaks, likely due to their anisotropy. All AuNPs were functionalized with PEG containing carboxylic acid groups, which conferred a negative surface charge indicated by ζ-potential around −28 mV. The longitudinal localized surface plasmon resonances (LSPR) were determined by UV-Visible spectroscopy to be 701 nm and 853 nm for short and long AuNRs, respectively, while the tip-confined LSPR for small and big AuNSs are 763 nm and 940 nm, respectively.

Even though the overall protein adsorption is known to be hindered by the functionalization of NPs with PEG, it cannot be fully suppressed and a certain amount of plasma proteins do adsorb on the NP surfaces, irrespective of the density and molecular weight of PEG coating.[37–40] In agreement with these previous findings, we found in the present study that PEGylated AuNPs are not completely inert and interact with plasma proteins upon intravenous administration in rodents.

To investigate the *in vivo* formation of protein corona, AuNPs were intravenously administered *via* tail injection in CD-1 mice and recovered by cardiac puncture, 10 min post-injection. Apart from being inexpensive, robust and readily available, CD-1 mice are an outbred strain, widely employed for biomedical research and are ideal as a general multipurpose model for safety and pharmacological testing.[41] Cardiac puncture is employed in order to collect a single, good quality and large amount of blood from the experimental animals.[42] Plasma was then prepared from the recovered blood by centrifugation. A protocol combining size exclusion chromatography and membrane ultrafiltration was used for the isolation of AuNP–corona complexes from unbound and loosely bound plasma proteins, as previously described (see the Experimental section for further details).

DLS and ζ-potential measurements after *in vivo* incubation demonstrated that, in all cases, the hydrodynamic diameter did not change significantly and the surface charge remained negative (Fig. 1A and B). These results are in agreement with previous studies suggesting that negatively charged NPs do not exclusively interact with positively charged proteins, as electrostatic interactions are not the only driving force behind NP–corona interactions.[24,25] Interestingly, only for 70 nm NRs and NSs the ζ-potential was shifted toward less negative values, suggesting preferential interaction with positively charged proteins. The presence of negatively charged proteins can be explained by a sequential model of protein binding, in which positively charged proteins initially bind the NP, followed by negatively charged ones.[24] In the case of nanorods, DLS measurements show that the initial distribution with two peaks merges into a single one upon interaction with proteins, which has been previously reported by E. Yeo[43] *et al*. for AuNRs of 46 × 20 nm incubated in human serum under *in vitro* conditions, and is likely related to a more spherical morphology upon protein adsorption.

Regarding the plasmonic response of AuNPs, it has been reported that *in vitro* interactions of AuNPs with plasma proteins lead to a 5–10 nm red-shift in the LSPR band of spherical AuNPs when recorded in a biological medium, due to an increase in the local refractive index around the particles.[44,45] We recorded the UV-Visible spectra before and after *in vivo* administration and recovery of AuNRs and AuNSs. As shown in Fig. 1C, no significant changes were observed in the LSPR position, except for a blue-shift in the case of 40 nm AuNSs, which may be related to partial reshaping of nanostars. The morphology of AuNSs involves highly energetic facets, which are likely to undergo reshaping unless properly stabilized by a suitable capping agent, typically containing thiol groups.[46] An example of a similar observation has been reported,[47] for AuNSs capped with polyvinylpyrrolidone (PVP), which readily reshaped by simply adding small amounts of CTAB. We investigated by TEM the reshaping of AuNSs as a result of their *in vivo* interactions with plasma proteins. As shown in Fig. 2, the TEM images of AuNSs (and AuNRs) after recovery and purification revealed well-dispersed NPs in the presence of protein molecules adsorbed onto their surface, as expected for protein corona formation. Several washing steps were performed to confirm that the PC–NP complex was correctly isolated from the free proteins (Fig. S1, ESI†). The TEM images confirm that 40 nm AuNSs had undergone reshaping, while AuNSs of 70 nm remained intact (Fig. S2 and S3, ESI†). As the conditions of the experiments have been the same for all NPs during the whole experiment, the reshaping process could be explained by the different sizes of the NPs. Even though AuNSs employed in this study are capped with thiolated PEG, the high molecular weight (10 kDa) is likely to lead to insufficient surface coverage for smaller AuNSs.

Proteins adsorbed on AuNPs *in vivo* were separated by Sodium Dodecyl Sulfate Polyacrylamide Gel Electrophoresis (SDS-PAGE) and visualized by Imperial Protein staining (Fig. 3A). The composition of protein coronas was found to quantitatively and qualitatively differ between the different types of AuNPs, as a first indication that the size and shape do influence the protein corona formation under *in vivo* blood-flow conditions. As illustrated in Fig. 3A, 70 nm AuNSs were found to adsorb a significantly larger amount of protein, which could be explained by the higher surface area that AuNSs exhibit as compared to their rod-like counterparts. Indeed, the SDS-PAGE results show that AuNSs adsorbed a larger amount of protein than AuNRs, which was further reinforced by the quantification of the total amount of protein adsorbed onto the different types of AuNPs, as illustrated in Fig. 3B.

A comprehensive comparison of the protein corona profiles for the different types of AuNPs was carried out by LC-MS/MS.

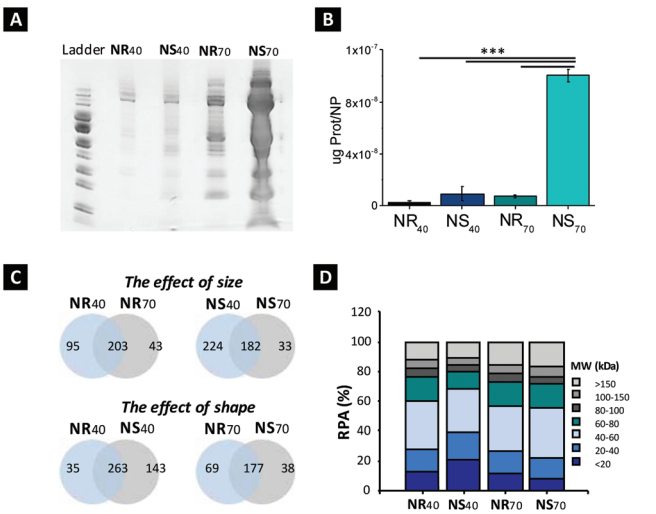

Fig. 3 Comparison of protein adsorption profiles on AuNPs after *in vivo* protein corona formation. (A) Comparison of the amount of proteins adsorbed onto AuNPs. The values of µg protein/NP represent the average and standard deviation from three independent experiments (n = 3 CD-1 mice per group; 4 independent experiments replicated). *** indicates $p < 0.001$. (B) Imperial protein stained SDS-PAGE gel of proteins associated with AuNPs *in vivo*. (C) Venn diagram displaying the number of unique proteins identified in the *in vivo* formed coronas, and their respective overlaps. (D) Classification of identified corona proteins, according to their molecular mass.

Table 1 Most abundant (top 20) proteins identified in the *in vivo* protein corona of AuNPs, as identified by LC-MS/MS. Relative protein abundance (RPA) values represent the average and standard deviation from three different experiments, each using n = 3 mice per group

NR40		NS40		NR70		NS70	
Identified protein	RPA	Identified protein	RPA	Identified protein	RPA	Identified protein	RPA
Serum albumin	5.16 ± 2.39	Serum albumin	3.71 ± 2.85	Serum albumin	7.52 ± 0.87	Serum albumin	8.19 ± 0.84
Alpha-2-macroglobulin	4.30 ± 0.64	Alpha-2-macroglobulin	3.70 ± 1.24	Alpha-2-macroglobulin	6.13 ± 0.37	Alpha-2-macroglobulin	7.80 ± 0.32
Fibrinogen beta chain	2.29 ± 0.90	Serine protease inhibitor A3K	2.44 ± 1.81	Serine protease inhibitor A3K	4.83 ± 0.86	Serine protease inhibitor A3K	6.01 ± 1.01
Apolipoprotein A–I	2.27 ± 0.22	Fibrinogen beta chain	2.37 ± 0.53	Apolipoprotein A–I	3.24 ± 0.47	Fibrinogen beta chain	3.99 ± 1.71
Complement factor H	2.12 ± 0.26	Apolipoprotein E	2.31 ± 0.37	Fibrinogen beta chain	2.51 ± 0.92	Alpha-1B-glycoprotein	3.11 ± 0.36
Serine protease inhibitor A3K	2.07 ± 1.06	Fibrinogen gamma chain	2.07 ± 0.25	Fibrinogen gamma chain	2.28 ± 0.92	Fibrinogen gamma chain	2.99 ± 1.48
Ig mu chain C region (fragment)	1.71 ± 0.29	Apolipoprotein A–I	1.98 ± 1.21	Complement C3	2.10 ± 0.34	Apolipoprotein A–I	2.57 ± 0.80
Fibrinogen gamma chain	1.64 ± 0.56	Ig mu chain C region (fragment)	1.87 ± 0.69	Apolipoprotein E	1.71 ± 0.23	Apolipoprotein E	1.98 ± 0.67
Argininosuccinate synthase	1.62 ± 0.54	Complement factor H	1.73 ± 0.17	Murinoglobulin-1	1.71 ± 0.10	Fibrinogen alpha chain	1.94 ± 0.74
Plasminogen	1.61 ± 0.20	If kappa light chain (fragment)	1.61 ± 0.05	Complement factor H	1.68 ± 0.38	Murinoglobulin-1	1.93 ± 0.17
Protein Ighv7-1 (fragment)	1.55 ± 0.28	Complement C3	1.33 ± 0.84	Ig mu chain C region (fragment)	1.67 ± 0.28	Complement factor H	1.63 ± 0.34
Apolipoprotein E	1.50 ± 0.45	IgM heavy chain VDJ region (fragment)	1.29 ± 0.54	Alpha-1B-glycoprotein	1.35 ± 0.31	Apoa1 protein	1.55 ± 2.69
Complement C3	1.49 ± 0.93	Beta-globin	1.13 ± 0.25	Fibronectin	1.28 ± 0.31	Complement C3	1.31 ± 0.18
Beta-globin	1.25 ± 0.08	Fibrinogen alpha chain	1.08 ± 0.22	Plasminogen	1.15 ± 0.10	Ig mu chain C region (fragment)	1.31 ± 0.58
Betaine–homocysteine *S*-methyltransferase 1	1.18 ± 0.45	Protein Ighv7-1 (fragment)	1.04 ± 0.52	Alpha-1-antitrypsin 1–3	1.13 ± 0.18	Ceruloplasmin	1.25 ± 0.21
Apolipoprotein C-III	1.18 ± 0.32	Argininosuccinate synthase	1.01 ± 0.45	Serpina1a protein	1.12 ± 0.07	Fibronectin	1.25 ± 0.35
Plasma kallikrein	1.17 ± 0.35	Complement factor properdin	0.94 ± 0.54	Fibrinogen alpha chain	1.09 ± 0.38	Serine protease inhibitor A3N	1.20 ± 0.24
Murinoglobulin-1	1.08 ± 0.12	Plasminogen	0.92 ± 0.26	Beta-globin	1.09 ± 0.27	Murinoglobulin-2	1.18 ± 0.28
Apolipoprotein C–I	1.04 ± 0.45	Plasma kallikrein	0.86 ± 0.24	Protein Ighv7-1 (fragment)	1.01 ± 0.22	Alpha-1-antitrypsin 1–3	1.16 ± 0.04
Fructose-bisphosphate aldolase B	1.04 ± 0.47	Fibronectin	0.85 ± 0.20	Ceruloplasmin	0.97 ± 0.19	Serpina1a protein	1.12 ± 0.03

The Venn diagrams displayed in Fig. 3C indicate the number of common and unique proteins identified after the digestion of corona-covered AuNPs of different sizes and shapes. Our results suggest that the total amount of adsorbed protein (Fig. 3B) does not necessarily reflect the complexity of the protein corona composition (Fig. 3C). For instance, even though a significantly larger amount of protein was found to adsorb onto 70 nm AuNSs as compared to 40 nm AuNSs, the total number of identified proteins was significantly higher in the case of 40 nm AuNSs (n = 406 for 40 nm AuNSs; n = 215 for 70 nm AuNSs). We hypothesize that the protein exchange and protein interaction are affected by the presence of the spikes, so that the shorter the spike, the easier the protein exchange will be, and as a consequence the higher the number of different proteins that are able to interact with the NP surface. On the other hand, reshaping of 40 nm AuNSs could more easily allow protein replacement, resulting in a higher complexity of their protein corona. In addition, 40 nm AuNSs also display a significantly higher number of different proteins than the corresponding 40 nm AuNRs, while having a similar total amount of adsorbed proteins. We thus find that small AuNPs show a more complex protein corona as compared to that on their larger counterparts. We however find an opposite behaviour for 70 nm NPs, where AuNRs seem to present a protein corona with a higher number of protein types than AuNSs of a similar size.

To better understand the effect of AuNP size and shape on the *in vivo* protein corona formation, the relative protein abundance (RPA) of each identified protein was calculated and surface-bound proteins were classified according to their molecular mass (Fig. 3D). Interestingly, 40 nm AuNSs present a significantly larger amount of proteins with MW < 20 kDa, and a slightly larger abundance of proteins with MW = 20–40 kDa than the other AuNPs. Previous studies by Pozzi *et al.*[48] and Hadjidemetriou *et al.*[31] on liposomal NPs show, under *in vitro* dynamics and *in vivo* conditions, respectively, a tendency toward interactions with low MW proteins. Our study is in agreement with this observation, as proteins with MW < 80 kDa contribute to 75–80% of the protein coronas for all AuNPs.

Table 1 summarizes the most abundant (top 20) proteins adsorbed onto the AuNP surface. Serum albumin was found to be the most abundant protein in all cases. The presence of serum albumin on the corona of AuNPs has been previously reported[40] for spherical AuNPs of different sizes *under in vitro* conditions. While preferential adsorption of opsonins such as immunoglobulins and complement proteins enhance phagocytosis, leading to NP removal from blood, serum albumin and apolipoproteins are known to extend blood circulation. The second most abundant protein for all AuNPs employed was found to be alpha-2-macroglobulin (A2M), a protease inhibitor and a cytokine transporter.[49] It is noteworthy that even though the two most abundant proteins are the same for all AuNPs, regardless of their size and shape, only 10 out of the top 20 proteins are common for all of them (those on the top 20 may be found in the total list of proteins), which have different RPA values depending on the NP type. For example, 40 nm AuNPs present argininosuccinate synthase and plasma kallikrein proteins within their top 20, whereas 70 nm AuNPs do not. In contrast, 70 nm AuNPs display alpha-1B-glycoproteins, ceruloplasmin, alpha-1-antitrypsin 1–3 and serpina1a proteins, which are not present in 40 nm AuNPs. This may mean that the NP size plays an important role in protein-nanoparticle interactions, such that some proteins show a higher tendency to attach to NPs, depending on their size.

It should however be kept in mind that the procedure applied for this study may pose certain limitations. First of all, it is not possible to recover all of the AuNPs injected into the mice and hence, the protein corona analysis is necessarily limited to the recovered NPs. Moreover, the recovery of proteins from metallic nanoparticles is a rather difficult task, as some proteins are difficult to detach from the NP surface without disruption. As a consequence, the analysis of PC composition is obviously limited to the proteins that could be effectively recovered.

In a broader context, we propose that the investigation and understanding of *in vivo* protein corona formation and composition are necessary toward the development of adequate gold-based nanoparticle systems for biomedical applications. Although usually seen as an obstacle, the protein corona also provides new opportunities such as NP manipulation to control their interaction with proteins, optimization of drug loading or discovery of biomarkers. Nevertheless, it is crucial to perform a comprehensive characterization of the protein corona under realistic *in vivo* conditions, in order to understand the interaction of NPs with the physiological media and its consequences.

Conclusions

We reported the *in vivo* observation of protein corona formation around anisotropic AuNPs. The effect of AuNP size and shape on the composition of the protein corona was thoroughly analysed, and protein adsorption profiles were determined for AuNSs and AuNRs with average sizes of 40 and 70 nm, upon intravenous administration in rodents. Our results demonstrate that both the total amount of protein adsorbed on AuNPs and the protein corona composition were affected by AuNP size and shape. Larger AuNSs were found to be covered by a significantly larger amount of proteins, as compared to other AuNPs, which we ascribe to their higher surface area. Our results suggest that the total amount of adsorbed protein does not necessarily reflect the complexity of the PC composition. We anticipate that comprehensive characterization of protein coronas under realistic *in vivo* conditions for different types of blood-injected pharmacological and imaging agents with nanoscale dimensions is necessary to improve our understanding of their overall clinical performance.

Experimental

Materials

Hydrogen tetrachloroaurate trihydrate ($HAuCl_4 \cdot 3H_2O$, ≥99.9%), trisodium citrate (≥98%), hexadecyltrimethylammonium bromide (CTAB, ≥99.0%), silver nitrate ($AgNO_3$, ≥99.0%), hydrochloric acid (HCl, 37%), L-ascorbic acid (AA, ≥99%) and sodium borohydride ($NaBH_4$, 99%) were purchased from Sigma-Aldrich. Mercapto-poly(ethylene glycol) carboxylic acid (α-Mercapto-ω-carboxy PEG, M_w 10K) was purchased from Rapp Polymere. Milli-Q water was used in all experiments. All glassware was washed with aqua regia, rinsed with water, and dried prior to use.

Synthesis of gold nanorods

Gold nanorods were prepared using Ag-assisted seeded growth.[33–35] Gold seeds were synthesized by fast reduction of $HAuCl_4$ (5 mL, 0.25 mM) with freshly prepared $NaBH_4$ (0.3 mL, 10 mM) in an aqueous CTAB solution (100 mM), under vigorous stirring. The color of the solution changed from yellow to brownish yellow and the seed solution was aged at 27 °C for 30 min before use, to promote the decomposition of sodium borohydride.

To prepare short AuNRs, an aliquot of seed solution (3 mL) was added to a growth solution containing CTAB (250 mL, 100 mM), $HAuCl_4$ (2.5 mL, 50 mM), ascorbic acid (1.88 mL, 100 mM) and $AgNO_3$ (2 mL, 5 mM). The mixture was gently shaken and left undisturbed at 30 °C for 1 h. The solution was centrifuged twice (8000 rpm, 30 min) to remove excess reactants and dispersed in the aqueous CTAB solution (100 mL, 1 mM). The average length and diameter (in nm) determined by measuring the dimensions from the TEM images was 39.5 ± 1.6 and 11.2 ± 0.9, respectively.

Long gold nanorods were prepared by adding an aliquot of seed solution (0.6 mL) to a growth solution containing CTAB (250 mL, 100 mM), $HAuCl_4$ (2.5 mL, 50 mM), HCl (4.75 mL, 1 M), ascorbic acid (2 mL, 100 mM) and $AgNO_3$ (3 mL, 10 mM). The mixture was gently shaken and left undisturbed at 30 °C for 2 h. The solution was centrifuged (6000 rpm, 30 min) to remove excess reactants and dispersed in the aqueous CTAB solution (100 mL, 1 mM). The average length and diameter (in nm) determined by measuring the dimensions from the TEM images was 70.4 ± 2.5 and 14.5 ± 1.1, respectively.

Synthesis of gold nanostars

Gold nanostars were prepared using a surfactant-free method assisted by silver ions.[36] A certain volume of ~14 nm gold seeds (3.75 mL and 5 mL for the preparation of 70 nm and 40 nm in diameter gold nanostars, respectively, [Au] = 0.5 mM) prepared by the Turkevich method[50] was added to an aqueous solution (250 mL) containing $HAuCl_4$ (1.25 mL, 50 mM) and HCl (0.25 mL, 1 M), followed by fast addition of $AgNO_3$ (0.75 mL, 10 mM) and AA (1.25 mL, 100 mM). After 30 s, an aqueous CTAB solution (3.75 mL, 100 mM) was added to the mixture to enhance the colloidal stability of AuNSs. Upon synthesis, the solution was centrifuged (3500 rpm, 30 min for 70 nm AuNSs, and 5000 rpm, 30 min for 40 nm AuNSs) to remove excess reactants, and dispersed in water (100 mL). The average diameter (in nm) determined by measuring the dimensions from the TEM images was 71.4 ± 1.9 and 42.3 ± 1.8, respectively.

Functionalization with α-Mercapto-ω-carboxy PEG

Mercapto poly (ethylene glycol) carboxylic acid with a molecular weight of 10 kg mol^{-1} was used for ligand exchange. An aqueous solution of PEG (20 mL) containing 50 molecules per nm^2 was added dropwise to the as-synthesized gold nanoparticles under vigorous stirring. The mixture was allowed to react for 1 h. PEG-modified gold nanoparticles were centrifuged twice (previous conditions) and finally dispersed in water.

Characterization

Transmission electron microscopy (TEM) images were obtained with a JEOL JEM-1400PLUS transmission electron microscope operating at an acceleration voltage of 120 kV using carbon-coated 400 square mesh copper grids. UV-vis optical extinction spectra were recorded using an Agilent 8453 UV-vis diode-array spectrophotometer.

Animal experiments

Eight to ten week old CD-1 female mice were purchased from Charles River (UK). All experiments were performed with prior approval from the UK Home Office under a project license (PPL 70/7763) and in strict compliance with the UK Home Office Code of Practice for the Housing and Care of Animals used in Scientific Procedures. Mice were housed in groups of five with free access to water and kept at a temperature of 19–22 °C and a relative humidity of 45–65%. Before performing the procedures, animals were acclimatized to the environment for at least 7 days.

In vivo protein corona protocol

CD-1 mice were anesthetized by the inhalation of isoflurane and AuNPs (3.6×10^{11} NPs) were administered intravenously *via* the lateral tail vein. Blood was recovered 10 min post-injection by cardiac puncture using K2EDTA coated blood collection tubes. Approximately 0.5–1.0 mL of blood was recovered from each mouse. Plasma was prepared by inverting 10 times the collection tubes to ensure the mixing of blood with K2EDTA and subsequent centrifugation for 12 min at 1300 RCF at 4 °C. The supernatant was collected into Protein LoBind Eppendorf tubes. For each AuNP type, the plasma sample was obtained by pooling together the blood of 3 mice to achieve a plasma volume of 1 mL. Three experimental replicates were performed and therefore 9 mice were used in total for each AuNP type.

Separation of PC-AuNPs from unbound proteins

PC–AuNP complexes recovered from blood were separated from unbound proteins by size exclusion chromatography, followed by membrane ultrafiltration. Immediately after recover-

ing from plasma/blood, 1 mL plasma samples were loaded onto a Sepharose CL-4B (Sigma Aldrich) column (15 × 1.5 cm) and equilibrated with Milli-Q water. A UV-vis spectrophotometer, Cary 50 Bio (Agilent Technologies), was used to detect the presence of AuNPs in fractions 4, 5 and 6. Fractions containing AuNPs were pulled together and concentrated to 500 μL by using a Vivaspin6 column (10 000 MWCO, Sartorious, Fischer Scientific) at 3000 rpm and 4 °C. Subsequently, a Vivaspin500 column (1 000 000 MWCO, Sartorious, Fischer Scientific) at 3000 rpm and 4 °C was used to further concentrate the sample to 100 μL and ensure an adequate separation of PC–AuNP complexes from any remaining unbound large proteins. PC–AuNPs were washed 8 times with 100 μL of Milli-Q water to remove weakly bound proteins.

Size distribution measurements by dynamic light scattering (DLS)

The AuNP hydrodynamic diameter was measured before and after protein corona formation using a Zetasizer Nano ZS (Malvern, Instruments, UK). For size distribution measurements, samples were diluted with Milli-Q water in cuvettes of 1 cm optical step. A minimum of 3 measurements per sample were made.

ζ-Potential measurements

The AuNP ζ-potential was measured before and after protein corona formation using a Zetasizer Nano ZS (Malvern, Instruments, UK). For ζ-potential measurements, the samples were diluted in 1 mL Milli-Q water and placed in Zetasizer disposable cuvettes. A minimum of 3 measurements per sample were made.

Determination of Au concentration by inductively coupled plasma mass spectrometry (ICP-MS)

The concentration of Au in the samples was determined by ICP-MS (Agilent 7500cx). Samples were digested in the presence of an aqua regia solution (HNO_3 cc : HCl cc; 1 : 3).

Transmission electron microscopy (TEM)

All AuNPs were visualized before and after protein corona formation in blood by TEM (FEI Tecnai 12 BioTwin). Samples were diluted prior to TEM observation and then, a drop from each colloid was placed onto a carbon-coated copper grid (CF-400 Cu, Electron Microscopy Science). Excess of suspension was removed using filter paper.

SDS-PAGE electrophoresis

Proteins associated with AuNPs (1×10^9 NPs) were mixed with 20 μL of Novex Tris-Glycine SDS Sample Buffer (2×, Thermo Scientific), 4 μL of NuPAGE sample reducing agent (10×, Thermo Scientific) and Milli-Q water for a final volume of 40 μL and boiled for 2–3 min at 90 °C. Samples were then loaded in Novex WedgeWell 4–20% Tris-Glycine MiniGel of 10 wells (Thermo Scientific) and the gel was run for 25–30 min at 225 mV in 10 times diluted Novex Tris-Glycine SDS Running Buffer (10×, Thermo Scientific). Staining was performed with an Imperial Protein Stain reagent (Thermo Scientific) for 1 h, followed by washing in Milli-Q water for 2–3 days.

Quantification of adsorbed proteins (BCA Assay)

Proteins adsorbed onto AuNPs were quantified by using a BCA Protein assay kit. Pb values, expressed as μg of protein per NP, were then calculated and plotted as the average ± standard error of three independent experiments. For the BCA assay, a calibration curve of 6 points was generated by serial dilutions of BSA in Milli-Q water, with the top standard at a concentration of 2 mg mL^{-1}. BCA reagents A and B were mixed at a ratio 50 : 1 and 200 μL of the BCA mixture were dispensed into 96 well-plates. Then, 25 μL of each standard or 2.5 μL of each sample was added to each well. The plate was incubated for 30 min at 37 °C and then the absorbance at 574 nm was recorded on a plate reader (Fluostar Omega). Protein concentrations were calculated according to the calibration curve. To quantify the Au concentration, ICP-MS (Agilent 7500xc) was used.

Mass spectrometry

Proteins associated with AuNPs (1×10^9 NPs) were mixed with 20 μL of Novex Tris-Glycine SDS Sample Buffer (2×, Thermo Scientific), 4 μL of NuPAGE Sample Reducing Agent (10×, Thermo Scientific) and Milli-Q water to a final volume of 40 μL and boiled for 2–3 min at 90 °C. Samples were then loaded in Novex WedgeWell 10% Tris-Glycine MiniGel of 10 wells (Thermo Scientific) and the gel was run for 3–5 min in 10 times diluted Novex Tris-Glycine SDS Running Buffer (10×, Thermo Scientific). Staining was performed with an Imperial Protein Stain reagent (Thermo Scientific) for 1 h and followed by washing in Milli-Q water for 2–3 days. Bands of interest were excised from the gel and dehydrated using acetonitrile, followed by vacuum centrifugation. Dried gel pieces were reduced with 10 mM dithiothreitol and alkylated with 55 mM iodoacetamide. Gel pieces were then washed alternately with 25 mM ammonium bicarbonate, followed by acetonitrile. This process was repeated, and the gel pieces were dried by vacuum centrifugation. Samples were digested with trypsin overnight at 37 °C. The digested samples were then analysed by LC-MS/MS using an UltiMateR 408 3000 Rapid Separation LC (RSLC, Dionex Corporation, Sunnyvale, CA) coupled to an Orbitrap Velos Pro (Thermo Fisher Scientific) mass spectrometer. Peptide mixtures were separated using a gradient from 92% A (0.1% FA in water) and 8% B (0.1% FA in acetonitrile) to 33% B, in 44 min at 300 nL min, using a 250 mm × 75 μm i.d. 1.7 μM BEH C18, analytical column (Waters). Peptides were automatically selected for fragmentation by data dependent analysis. Data produced were searched using Mascot (Matrix Science UK), against the [*SwissProt*] database with taxonomy of [*mouse*] selected. The Scaffold software (version 4.3.2, Proteome Software Inc.) was used to validate MS/MS based peptide and protein identifications and for relative quantification based on spectral counting. Peptide identifications were accepted if they could be established at greater than 95.0% probability by using the Peptide Prophet algorithm with

Scaffold delta-mass correction. Protein identifications were accepted if they could be established at greater than 99.0% probability and contained at least 2 identified peptides. Protein probabilities were assigned by using the Protein Prophet algorithm. Proteins that contained similar peptides and could not be differentiated based on MS/MS analysis alone were grouped to satisfy the principles of parsimony. Semi quantitative assessment of the protein amounts was conducted using normalized spectral countings, NSCs, provided by Scaffold Software. The mean value of NSCs obtained in the three experimental replicates for each protein was normalized to the protein MW and expressed as a relative quantity by applying the following equation:

$$\mathrm{MWNSC_k} = \frac{(\mathrm{NSC/MW})_\mathrm{k}}{\sum_{i=1}^{N} (\mathrm{NSC/MW})_\mathrm{i}} \times 100$$

where $\mathrm{MWNSC_k}$ is the percentage molecular weight normalized NSC for protein k and MW is the molecular weight in kDa for protein k. This equation takes into consideration the protein size and evaluates the contribution of each protein reflecting its relative protein abundance (RPA).

Statistical analysis

Data statistical analysis was carried out using IBM SPSS Statistics software. One-way analysis of variance (ANOVA) followed by the Tukey multiple comparison test were used and p values < 0.05 were considered significant.

Conflicts of interest

There are no conflicts to declare.

Acknowledgements

LML-M acknowledges funding from the Spanish MINECO (Grant #MAT2013-46101R). The authors also wish to thank the staff in the Faculty of Life Sciences EM Facility for their assistance and the Welcome Trust for equipment grant support to the EM Facility. In addition, the assistance of Mass Spectrometry Facility staff at the University of Manchester is acknowledged.

Notes and references

1 T. Cedervall, I. Lynch, S. Lindman, T. Berggård, E. Thulin, H. Nilsson, K. A. Dawson and S. Linse, *Proc. Natl. Acad. Sci. U. S. A.*, 2007, **104**, 2050–2055.
2 D. Chen, S. Ganesh, W. Wang and M. Amiji, *Nanomedicine*, 2017, **12**, 2113–2135.
3 G. Caracciolo, O. C. Farokhzad and M. Mahmoudi, *Trends Biotechnol.*, 2017, **35**, 257–264.
4 M. P. Monopoli, C. Åberg, A. Salvati and K. A. Dawson, *Nat. Nanotechnol.*, 2012, **7**, 779–786.
5 M. Lundqvist, J. Stigler, G. Elia, I. Lynch, T. Cedervall and K. A. Dawson, *Proc. Natl. Acad. Sci. U. S. A.*, 2008, **105**, 14265–14270.
6 M. M. Yallapu, N. Chaunan, S. F. Othman, V. Khalilzad-Sharghi, M. C. Ebeling, S. Khan, M. Jaggi and S. C. Chauhan, *Biomaterials*, 2015, **46**, 1–12.
7 J. Saikia, M. Yazdimamaghani, S. P. Hadipour-Moghaddam and H. Ghandehari, *ACS Appl. Mater. Interfaces*, 2016, **8**, 34820–34832.
8 D. Pozzi, G. Caracciolo, A. L. Capriotti, C. Cavaliere, G. La Barbera, T. J. Anchordoquy and A. Laganà, *J. Proteomics*, 2015, **119**, 209–217.
9 V. Colapicchioni, M. Tilio, L. Digiacomo, V. Gambini, S. Palchetti, C. Marchini, D. Pozzi, S. Occhipinti, A. Amici and G. Caracciolo, *Int. J. Biochem. Cell Biol.*, 2016, **75**, 180–187.
10 V. Mirshafiee, R. Kim, M. Mahmoudi and M. L. Kraft, *Int. J. Biochem. Cell Biol.*, 2016, **75**, 188–195.
11 S. Schöttler, K. Klein, K. Landfester and V. Mailänder, *Nanoscale*, 2016, **8**, 5526–5536.
12 A. Solorio-Rodríguez, V. Escamilla-Rivera, M. Uribe-Ramírez, A. Chagolla, R. Winkler, C. M. García-Cuellar and A. De Vizcaya-Ruiz, *Nanoscale*, 2017, **9**, 13651–13660.
13 S. Zanganeh, R. Spitler, M. Erfanzadeh, A. M. Alkilany and M. Mahmoudi, *Int. J. Biochem. Cell Biol.*, 2016, **75**, 143–147.
14 M. Mahmoudi, I. Lynch, M. R. Ejtehadi, M. P. Monopoli, F. B. Bombelli and S. Laurent, *Chem. Rev.*, 2011, **111**, 5610–5637.
15 P. K. Jain, K. S. Lee, I. H. El-Sayed and M. A. El-Sayed, *J. Phys. Chem. B*, 2006, **110**, 7238–7248.
16 S. Eustis and M. A. El-Sayed, *Chem. Soc. Rev.*, 2006, **35**, 209–217.
17 D. A. Giljohann, D. S. Seferos, W. L. Daniel, M. D. Massich, P. C. Patel and C. A. Mirkin, *Angew. Chem., Int. Ed.*, 2010, **49**, 3280–3294.
18 S. Ashraf, B. Pelaz, P. Del Pino, M. Carril, A. Escudero, W. J. Parak, M. G. Soliman, Q. Zahng and C. Carrillo-Carrión, *Top. Curr. Chem.*, 2016, **370**, 169–202.
19 A. C. Anselmo and S. Mitragotri, *AAPS J.*, 2015, 1041–1054.
20 D. Docter, D. Westmeier, M. Markieeicz, S. Stolte, S. K. Knauer and R. H. Stauber, *Chem. Soc. Rev.*, 2015, **44**, 6094–6121.
21 C. Carnovale, G. Bryant, R. Shukla and V. Bansal, *Prog. Mater. Sci.*, 2016, **83**, 152–190.
22 Z. Ma, J. Bai, Y. Wang and X. Jianq, *ACS Appl. Mater. Interfaces*, 2014, **6**, 2431–2438.
23 Z. J. Deng, G. Mortimer, T. Schiller, A. Musumeci, D. Martin and R. F. Minchin, *Nanotechonology*, 2009, **20**, 455101–455110.
24 M. A. Dobrovolskaia, A. K. Patri, J. Zheng, J. D. Clogston, N. Ayub, P. Aggarwal, B. W. Neun, J. B. Hall and S. E. McNeil, *Nanomedicine*, 2009, **5**, 106–117.
25 M. Schäffler, M. Semmler-Behnke, H. Sariouglu, S. Takenaka, A. Wenk, C. Schleh, S. M. Hauck,

B. D. Johnston and W. G. Kreyling, *Nanotechnology*, 2013, **24**, 265103–265112.
26 J. Piella, N. G. Bastús and V. Puntes, *Bioconjugate Chem.*, 2017, **28**, 88–97.
27 H. Cai, Y. Ma, Z. Wu, Y. Ding, P. Zhang, X. He, J. Zhou, Z. Chai and Z. Zhang, *NanoImpact*, 2016, **3**, 40–46.
28 J. C. Y. Kah, C. Grabinski, E. Untener, C. Garrett, J. Chen, D. Zhu, S. M. Hussain and K. Hamad-Schifferli, *ACS Nano*, 2014, **8**, 4608–4620.
29 A. D'Hollander, H. Jans, G. V. Velde, C. Verstraete, S. Massa, N. Devoogdt, T. Stakenborg, S. Muyidermans, L. Lagae and U. Himmelreich, *Biomaterials*, 2017, **123**, 15–23.
30 M. Hadjidemetriou and K. Kostarelos, *Nat. Nanotechnol.*, 2017, **12**, 288–290.
31 M. Hadjidemetriou, Z. Al-Ahmady, M. Mazza, R. F. Collins, K. Dawson and K. Kostarelos, *ACS Nano*, 2015, **9**, 8142–8156.
32 M. Hadjidemetriou, Z. Al-Ahmady and K. Kostarelos, *Nanoscale*, 2016, **8**, 6948–6957.
33 M. Liu and P. Guyot-Sionnest, *J. Phys. Chem. B*, 2005, **109**, 22192–22200.
34 B. Nikoobakht and M. A. El-Sayed, *Chem. Mater.*, 2003, **15**, 1957–1962.
35 L. Scarabelli, A. Sánchez-Iglesias, J. Pérez-Juste and L. M. Liz-Marzán, *J. Phys. Chem. Lett.*, 2015, **6**, 4270–4279.
36 H. Yuan, C. G. Khoury, H. Hwang, C. M. Wilson, G. A. Grant and T. Vo-Dinh, *Nanotechonology*, 2012, **23**, 075102–075111.
37 D. Pozzi, V. Colapicchioni, G. Caracciolo, S. Piovesana, A. L. Capriotti, S. Palchetti, S. De Grossi, A. Riccioli, H. Amenitsch and A. Laganà, *Nanoscale*, 2014, **6**, 2782–2792.
38 M. A. Dobrovolskaia, B. W. Neun, S. Man, X. Ye, M. Hansen, A. K. Patri, R. M. Crist and S. E. McNeil, *Nanomedicine*, 2014, **10**, 1453–1463.
39 R. Gref, M. Lück, P. Quellec, M. Marchand, E. Dellacherie, S. Harnisch, T. Blunk and R. H. Müller, *Colloids Surf., B*, 2000, **3**, 301–313.
40 S. Schöttler, G. Becker, S. Winzen, T. Steinbach, K. Mohr, K. Landfester, V. Mailänder and F. R. Wurm, *Nat. Nanotechnol.*, 2016, **11**, 372–377.
41 R. Chia, F. Achilli, M. F. W. Festing and E. M. C. Fisher, *Nat. Genet.*, 2005, **37**, 1181–1186.
42 S. Parasuraman, R. Raveendran and R. Kesavan, *J. Pharmacol. Pharmacother.*, 2010, **1**, 87–93.
43 E. L. L. Yeo, J. U.-J. Cheah, B. Y. Lim, P. S. P. Thong, K. C. Soo and J. C. Y. Kah, *ACS Biomater. Sci. Eng.*, 2017, **3**, 1039–1050.
44 G. Maiorano, S. Sabella, B. Sorce, V. Brunetti, M. A. Malvindi, R. Cingolani and P. P. Pompa, *ACS Nano*, 2010, **4**, 7481–7491.
45 A. L. Chen, M. A. Jackson, A. Y. Lin, E. R. Figueroa, Y. S. Hu, E. R. Evans, V. Asthana, J. K. Young and R. A. Drezek, *Nanoscale Res. Lett.*, 2016, **11**, 303–315.
46 Y. Wang, A. B. Serrano, K. Sentosun, S. Bals and L. M. Liz-Marzán, *Small*, 2015, **11**, 4314–4320.
47 L. Rodríguez-Lorenzo, J. M. Romo-Herrera, J. Pérez-Juste, R. A. Alvarez-Puebla and L. M. Liz-Marzán, *J. Mater. Chem.*, 2011, **21**, 11544–15549.
48 S. Palchetti, D. Pozzi, A. L. Capriotti, G. Barbera, R. Z. Chiozzi, L. Digiacomo, G. Peruzzi, G. Caracciolo and A. Laganà, *Colloids Surf., B*, 2017, **153**, 263–271.
49 J. Schaller, S. Gerber, U. Kampfer, S. Lejon and C. Trachsel, *Human Blood Plasma Proteins: Structure and Function*, Wiley, New York, 2008.
50 J. Turkevich, P. C. Stevenson and J. Hillier, *Discuss. Faraday Soc.*, 1951, **11**, 55–75.

